

GROMMET: an N -body code for high-resolution simulations of individual galaxies

John Magorrian^{*}

Rudolf Peierls Centre for Theoretical Physics, 1 Keble Road, Oxford OX1 3NP

ABSTRACT

This paper presents a fast, economical particle-multiple-mesh N -body code optimized for large- N modelling of collisionless dynamical processes, such as black-hole wandering or bar-halo interactions, occurring within isolated galaxies. The code has been specially designed to conserve linear momentum. Despite this, it also has variable softening and an efficient block-timestep scheme: the force between any pair of particles is calculated using the finest mesh that encloses them both (respecting Newton’s third law) and is updated only on the longest timestep of the two (which conserves momentum). For realistic galaxy models with $N \gtrsim 10^6$, it is faster than the fastest comparable momentum-conserving tree code by a factor ranging from ~ 2 (using single timesteps) to ~ 10 (multiple timesteps in a concentrated galaxy).

Key words:

1 INTRODUCTION

Newton’s third law is a central pillar of physics. Much of what we know about the dynamical evolution of galaxies comes from N -body simulation, but most N -body codes use approximations that break the third law. A well-known example of the consequences of breaking it is provided by the sinking satellite problem (Hernquist & Weinberg 1989; Weinberg 1989; Velazquez & White 1999); the dynamical friction felt by the satellite is grossly overestimated if one “pins” the centre of the host galaxy, ignoring the galaxy’s $l = 1$ dipole response. This example is perhaps extreme, but there are many other situations where one is interested in the detailed response of a galaxy to asymmetric perturbations and would like to be able to model it without having to worry about artifacts arising from violations of Newton’s third law. Examples include modelling bar-halo interactions (see McMillan & Dehnen (2005) and references therein) and the wandering of central supermassive black holes.

This paper describes the N -body code GROMMET (GRavity On Multiple Meshes Economically and Transparently), which has been designed specifically to model the detailed dynamical evolution of individual galaxies without using any approximations that violate Newton’s third law. I assume that the galaxy is collisionless. It is completely described by a distribution function (DF) $f(\mathbf{x}, \mathbf{v}; t)$, which gives the (mass) density of particles in phase space, along with the potential $\Phi(\mathbf{x}; t)$ generated by this DF and any external sources. The evolution of f is governed by the col-

lisionless Boltzmann equation (CBE),

$$\frac{\partial f}{\partial t} + \mathbf{v} \cdot \nabla f + \mathbf{a} \cdot \frac{\partial f}{\partial \mathbf{v}} = 0, \quad (1)$$

where the accelerations $\mathbf{a} \equiv -\partial\Phi/\partial\mathbf{x}$. As Hernquist & Ostriker (1992) and Leeuw, Combes & Binney (1993) emphasise, in a collisionless N -body code particles are not to be thought of as representing stars or groups of stars. Instead one is using the method of characteristics to integrate (1), estimating the accelerations $\mathbf{a}(\mathbf{x})$ by Monte Carlo sampling. Of course, the shot noise in these estimates means that in practice any simulation will never be perfectly collisionless. Therefore it is important to make N as large as possible in order to minimize the effects of this noise. So, GROMMET has been designed to be both fast and economical on memory.

In section 2 below I describe the multiple-mesh procedure used by GROMMET to estimate accelerations. Section 3 shows how this leads naturally to a momentum-conserving block-timestep integrator based on Duncan, Levison & Lee’s (1998) potential-splitting scheme. In section 4 I present the results of some tests and also compare GROMMET’s performance against other codes’. Section 5 sums up. For completeness, I include in an Appendix an explanation of James’ (1977) method, which is used in Section 2.

2 POTENTIAL SOLVER

The task of the potential solver in a collisionless N -body code is to estimate the accelerations

$$\mathbf{a}(\mathbf{x}) = -\nabla \int \frac{G\rho(\mathbf{x}')}{|\mathbf{x} - \mathbf{x}'|} d^3\mathbf{x}', \quad (2)$$

^{*} E-mail: magog@thphys.ox.ac.uk

where one does not know the density distribution $\rho(\mathbf{x})$ explicitly, but instead only has a discrete sample of N particles with positions \mathbf{x}_i and masses m_i drawn from it.

2.1 Particle-mesh method

At the heart of GROMMET's potential solver is the particle mesh (PM) method (Hockney & Eastwood 1988). It uses a cubical mesh, with vertices at positions \mathbf{x}_{ijk} , spaced a distance h apart. The procedure for obtaining an initial estimate of the accelerations (eq. 2) felt by each particle follows.

(i) Loop over all N particles using cloud-in-cell interpolation to build up the discretized density distribution $\rho_{ijk} = \rho(\mathbf{x}_{ijk})$;

(ii) Calculate the potential Φ_{ijk} corresponding to this ρ_{ijk} using James' (1977) method (see Appendix);

(iii) Looping again over all N particles, use a finite-difference approximation to estimate accelerations $-\partial\Phi/\partial\mathbf{x}$ at the mesh points surrounding each particle, then interpolate the value of the acceleration at the particle's location using the same cloud-in-cell scheme employed in step (i).

Since steps (i) and (iii) use the same interpolation scheme, this procedure produces accelerations that obey Newton's third law subject to one extra condition: the finite-difference scheme in step (iii) cannot provide meaningful accelerations for particles that lie in the outermost layer of mesh cells, which means that those particles should be omitted in step (i). This seems an almost trivial point, but it is important for the refinement scheme introduced below. It turns out that for the scheme below to work properly we have to peel off the outer *two* layers of cells. I typically use meshes with 64^3 or 128^3 cells, of which then only 60^3 or 124^3 are assignable in step (i).

Apart from respecting Newton's third law, the other attractive features of the PM method are its efficiency and its linear scaling with N : the time needed to carry out step (ii) is independent of N , but for a typical mesh with 64^3 cells the overall time is dominated by the $\mathcal{O}(N)$ cost of carrying out the assignment steps (i) and (iii) once $N \gtrsim 5 \times 10^5$; similarly, the memory needed to store mesh quantities and to carry out James' method is negligible compared to that used for storing the particles' masses, positions and accelerations.

The major disadvantage of the PM method is that it does not work well for centrally concentrated mass distributions, since each particle has an effective size of order the mesh spacing h . In other words, the mesh spacing sets the effective softening length used in the calculation of the forces.

2.2 Refinement scheme

The natural remedy of this shortcoming is to introduce finer submeshes in interesting, higher-density regions and to recalculate the accelerations for particles inside each submesh. But how best to include the effect of the parent mesh's gravity field on the accelerations calculated in each submesh and vice versa? One possibility is to solve Poisson's equation on the submesh subject to boundary conditions interpolated from the parent mesh (e.g., Anninos, Norman & Clarke 1994; Jessop, Duncan & Chau 1994). This is a key element of

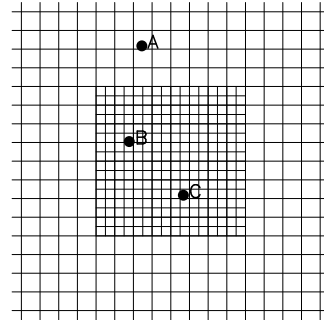


Figure 1. An example of the multiple mesh scheme used to calculate accelerations. Particles A, B and C all lie within the region covered by the outer, coarse mesh, but B and C also lie inside the fine, inner mesh. An initial estimate of the forces on all three particles comes from using the PM method on the coarse mesh. This is refined by isolating those particles within the inner mesh, recalculating their interparticle forces first using the fine mesh, then using the coarse, and adding the difference to the initial coarse-mesh estimate. Therefore, the force between A and each of B and C is obtained using the coarse mesh, but that between B and C comes from the fine mesh. In all cases Newton's third law is respected.

the widely-used family of multigrid methods (e.g., Kravtsov, Klypin & Khokhlov 1997; Knebe, Green & Binney 2001), and would be straightforward to apply in GROMMET using the method of equivalent charges (see Appendix). However, all of these schemes violate Newton's third law, as one can easily see by considering the force between a particle inside a submesh and another one outside.

GROMMET instead uses a simplified version of the scheme proposed by Gelato, Chernoff & Wasserman (1997) (see also figure 1). The acceleration felt by each particle is calculated using a series of nested "boxes". We start with the outermost toplevel box, which discretizes the simulation volume into, say, $n_x \times n_y \times n_z = 60^3$ assignable cells. This box, like any other box, can contain zero, one or more subboxes. Each subbox contains two meshes: a coarse one composed of an $(n_x/2) \times (n_y/2) \times (n_z/2)$ subblock of the parent's cells, and a fine one that covers the same subblock twice as finely in each direction, with $n_x \times n_y \times n_z$ cells.

For the most common situation in which each box contains no more than one subbox, the acceleration at any position \mathbf{x} is given by the sum over all boxes,

$$\mathbf{a}(\mathbf{x}) = \sum_j \mathbf{a}_j(\mathbf{x}), \quad (3)$$

where the contribution from the j^{th} box,

$$\mathbf{a}_j(\mathbf{x}) = \mathbf{a}_j^+(\mathbf{x}) - \mathbf{a}_j^-(\mathbf{x}), \quad (4)$$

is the difference between accelerations calculated using the PM method on the box's fine (+) and coarse (-) meshes, simply ignoring any particles that lie outside. The outermost toplevel box ($j = 0$) has no coarse mesh, so $\mathbf{a}_0^- = 0$. In this scheme the acceleration between any two particles is calculated using the box with the finest mesh spacing that encloses them both and Newton's third law is obeyed to machine precision. This last feature comes at a cost though: the acceleration (3) is discontinuous at box boundaries, a point to which I return below.

Sometimes one might want to refine a region that cannot be enclosed within a single subbox. If one simply tiles the region using, say, two abutting subboxes, the force between particles located at either side of the boundary between them will be calculated using the coarse parent mesh, which is usually not desirable. The solution is to let the subboxes overlap by a few mesh cells and then correct eq. (3) for the double counting of particles in the overlap region by introducing a third subbox whose boundaries are given by the intersection of the two overlapping subboxes and subtracting the accelerations (4) obtained in this new subbox. In contrast, Gelato, Chernoff & Wasserman (1997) introduce a buffer zone around each box and treat particles in the buffer zone differently from the rest. Their scheme violates Newton’s third law.

I have deliberately omitted any automated scheme for deciding where and when to introduce subboxes; these schemes inevitably break time-reversibility, and, for the type of problem the code was designed for, I expect that the user will already have a much better idea of how best to place boxes.

3 MOVING PARTICLES

The characteristic equation of the CBE is

$$\frac{dt}{1} = \frac{d\mathbf{x}}{\mathbf{v}} = \frac{d\mathbf{v}}{\mathbf{a}}, \quad (5)$$

where the accelerations $\mathbf{a}(\mathbf{x}, t)$ depend on the DF f through eq. (2). The most straightforward and widely used way of following the characteristics is by using a leapfrog integrator. The (fixed-timestep) leapfrog produces an approximate solution to (5) that respects many of its important symmetries; it is symplectic¹, reversible in time and, when the accelerations are obtained using a potential solver that respects Newton’s third law, it conserves linear momentum.

An unattractive feature of the leapfrog is that it uses the same fixed timestep for all particles. Consider a deeply plunging radial orbit in a model galaxy with a central density cusp or black hole. Integrating this orbit accurately near pericentre requires a very small timestep, which, in the standard leapfrog scheme, means that all other particles have to be integrated using the same small timestep, even those on loosely bound circular orbits. This can be prohibitively expensive, since it involves calculating the full set of accelerations $\mathbf{a}(\mathbf{x}, t)$ for all particles at every timestep.

GROMMET uses a block-timestep scheme to improve efficiency. Each of the boxes of section 2 above has an associated timestep, which can be chosen to be either equal to that of its parent box or a factor of two shorter. Broadly speaking, a particle’s position and velocity are updated using the shortest timestep of any of the boxes enclosing it, but the force between any pair of particles is updated only on the timestep of the longest particle, thus conserving linear momentum. The rest of this section makes this somewhat vague description more precise.

3.1 The standard leapfrog integrator

Recall that a leapfrog integrator with a single, fixed timestep τ corresponds to motion in a time-dependent Hamiltonian (e.g., Wisdom & Holman 1991)

$$H = T + \sum_{k=-\infty}^{\infty} \delta_{\epsilon} \left(k - \frac{t}{\tau} \right) V(\mathbf{x}_1, \dots, \mathbf{x}_N), \quad (6)$$

where $T \equiv \frac{1}{2} \sum_i m_i v_i^2$ is the kinetic energy of all the particles and $\delta_{\epsilon}(x) \equiv \frac{1}{2}(\delta(x - \epsilon) + \delta(x + \epsilon))$ with $0 < \epsilon \ll 1$. The periodic comb of delta functions turns on the potential energy $V(\mathbf{x}_1, \dots, \mathbf{x}_N)$ only at times $t = (k \pm \epsilon)\tau$ for integer k . Integrating the resulting equations of motion from time $t = k\tau$ to $t = (k + 1)\tau$ yields

$$\mathbf{v}_i(k + \frac{1}{2}) = \mathbf{v}_i(k) + \frac{1}{2}\tau \mathbf{a}_i(k), \quad (7)$$

$$\mathbf{x}_i(k + 1) = \mathbf{x}_i(k) + \tau \mathbf{v}_i(k + \frac{1}{2}), \quad (8)$$

$$\mathbf{v}_i(k + 1) = \mathbf{v}_i(k + \frac{1}{2}) + \frac{1}{2}\tau \mathbf{a}_i(k + 1), \quad (9)$$

where the accelerations $\mathbf{a}_i(k) \equiv -\partial V / m_i \partial \mathbf{x}_i$ evaluated at time $t = k\tau$. This is just the sequence of steps for the kick-drift-kick form of the leapfrog: the potential is turned on briefly just after $t = k\tau$ resulting in a “kick” (denoted K) to the particles’ velocities; the particles then “drift” (D) along at their new velocities until the potential turns on again just before $t = (k + 1)\tau$, at which point they receive another kick. The drift-kick-drift form of the leapfrog can be obtained by adding $\frac{1}{2}$ to the argument of the delta functions or, alternatively, by integrating the equations of motion from $(k - \frac{1}{2})\tau$ to $(k + \frac{1}{2})\tau$ instead.

Another way of looking at each of these versions of the leapfrog is to consider them as compositions of the two time-asymmetric first-order symplectic integrators (each applied left to right), $K(\tau/2)D(\tau/2)$ and $D(\tau/2)K(\tau/2)$, whose first-order error terms cancel (e.g., Saha & Tremaine 1992). In the following I write the leapfrogs as the sequence of operations $KDDK$ and $DKKD$, dropping the $(\tau/2)$ arguments.

3.2 A block-timestep leapfrog

In GROMMET the accelerations $\mathbf{a}(\mathbf{x})$ are given by a sum (3) of contributions (4) from boxes with different spatial refinement levels. The outermost box is associated with a timestep τ_0 and timestep level $l = 0$. Each subbox has a timestep $\tau_l = 2^{-l}\tau_0$ with timestep level l either equal to that of its parent or larger by one. Let us add together all the contributions (4) to $\mathbf{a}(\mathbf{x})$ from boxes having timestep level l and write the result as $\mathbf{a}_{(l)}(\mathbf{x})$. Let $V_{(l)}(\mathbf{x})$ be the corresponding contribution to the potential energy. Instead of turning on the full potential $V = \sum_l V_{(l)}$ at every timestep, consider the alternative Hamiltonian

$$H = T + \sum_{l=0}^{l_{\max}} \sum_{k=-\infty}^{\infty} \delta_{\epsilon} \left(k - \frac{t}{2^{-l}\tau_0} \right) V_{(l)}(\mathbf{x}_1, \dots, \mathbf{x}_N), \quad (10)$$

where l_{\max} is the maximum timestep refinement level and each $V_{(l)}$ is turned on only at times $t = 2^{-l}k\tau_0$. This is a variant of the potential splitting used by Duncan, Levison & Lee (1998) to model close encounters in planetary systems.

Integrating the equations of motion for this new Hamiltonian results in a nested sequence of $KDDK$ leapfrog

¹ This assumes that the accelerations are smooth, which is not the case for many collisionless N -body codes, including GROMMET.



Figure 2. The sequence of steps for motion in the Hamiltonian (10) with two levels of timestep refinement. For any given timestep level l , the K operation “kicks” particles inside any boxes having that timestep level, applying to each an impulse $\frac{1}{2}\tau_l \cdot (-\partial V_{(l)}/\partial \mathbf{x})$, where the timestep $\tau_l = 2^{-l}\tau_0$. These impulses change the particles’ velocities, but not their positions. They conserve the particles’ total linear momentum. The D operation “drifts” all particles for a time $\frac{1}{2}\tau_l$, changing their positions but not their velocities.

steps, as shown in figure 2. The sequence can be produced using the following simple recursive algorithm:

```

Step( $l, \tau$ ):
  if  $l > l_{\max}$ :
    Drift( $\tau/2$ )
  else:
    Kick( $l, \tau/2$ )
    Step( $l+1, \tau/2$ )
    Step( $l+1, \tau/2$ )
    Kick( $l, \tau/2$ )

```

This algorithm is called initially with $l = 0$ and $\tau = \tau_0$. Each Kick($l, \tau/2$) operation applies an impulse $-\frac{1}{2}\tau \nabla V_{(l)}$ to all particles, which changes the particles’ velocities but not their positions. The Drift operation moves the particles once the complete set of impulses has been applied.

This algorithm requires a factor $\sim l_{\max}$ fewer kick operations (and therefore fewer expensive force evaluations) than a simple leapfrog with a single timestep $2^{-l_{\max}}\tau_0$. It is obvious that it conserves linear momentum and is reversible in time. Unlike the integrator in Duncan, Levison & Lee (1998), however, it is *not* symplectic; the discontinuities in the accelerations at box boundaries mean that the Poincaré integral invariants are not conserved.

4 TESTS AND COMPARISONS

I have carried out a number of simple tests with small numbers of particles ($1 < N \lesssim 20$) to confirm that my implementation of the ideas above really does respect Newton’s third law and conserve linear momentum. These small- N tests serve only as minimal sanity checks; as stressed by Knebe, Green & Binney (2001), truly interesting tests of a collisionless code come not from testing how faithfully it reproduces the solution to the two-body problem, but rather from its ability to model collisionless systems accurately using large numbers of particles.

In this section I use some simple collisionless galaxy models to test GROMMET’s potential solver and integrator, comparing results obtained from GROMMET against those obtained from two other codes. Both of the other codes are available as part of the NEMO package. The first is the fast tree code described in Dehnen (2002). It obtains accelerations from a Cartesian multipole expansion. This respects Newton’s third law and a standard leapfrog integrator built around this potential solver then naturally conserves linear momentum. (A multiple-timestep version is also available, but it does not conserve momentum.) The second code (Hernquist & Ostriker 1992) uses the so-called “self-consistent field” (SCF) method, which represents the density and potential using a truncated basis function ex-

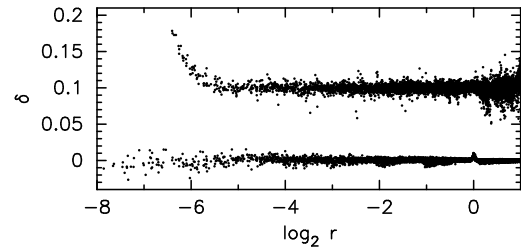


Figure 3. Fractional errors in the accelerations at randomly selected positions within and around an $N = 10^7$ -particle realization of a truncated power-law sphere. The lower set of points plot results calculated using the potential solver of section 2 using 8 levels of refinement of a 60^3 mesh with $x_{\max} = 2$. The upper set (offset by 0.1 vertically) are for results obtained using a tree code with fixed softening length $\epsilon = 10^{-2}$.

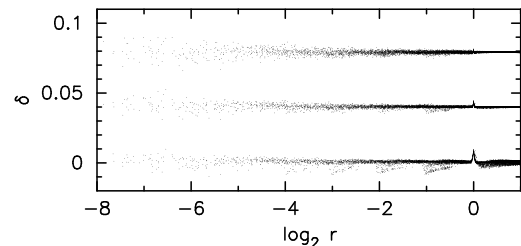


Figure 4. Fractional errors in the accelerations inside a 10^8 -particle realization of a power-law sphere, a factor of 10 more particles than in figure 3. The lower set of points plot results obtained using the potential solver of section 2 with the same set of nested boxes and 60^3 mesh employed for figure 3. The middle and upper set show the effects of using finer meshes with 124^3 (middle) and 252^3 (upper) cells, offset by 0.04 and 0.08 respectively.

pansion. It shows no respect for Newton’s third law, but, like GROMMET, is optimized for modelling single galaxies.

4.1 Static tests

Real galaxies have steep central density cusps (e.g., Lauer et al. 1995), so an obvious test of the potential solver is to check the accelerations it returns for an N -body realization of a truncated power-law sphere with density profile

$$\rho(r) \propto \begin{cases} r^{-\alpha}, & \text{if } r < r_{\max}, \\ 0, & \text{otherwise.} \end{cases} \quad (11)$$

I have generated a realization with $r_{\max} = 1$, $\alpha = 2$ having 10^7 equal-mass particles and used eq. (3) to calculate accelerations at randomly selected positions inside and around

the sphere. For this I use a toplevel box enclosing the region $|\mathbf{x}| < 2$ together with eight levels of refinement, the boundary of the i^{th} subbox being given by $|\mathbf{x}| = 2^{1-i}$. Figure 3 plots the fractional difference between the results of this procedure against the exact, analytical expression for the acceleration. For radii $2^{-5} < r < 1$ the RMS fractional error is only 0.0023, rising to 0.007 for $2^{-8} < r < 2^{-5}$, within which there are relatively few particles. The source of this good and desirable behaviour is the decrease in the effective softening length as one moves to smaller length scales.

For comparison, the upper set of points in figure 3 plot the errors in the accelerations of the same 10^7 -particle sphere calculated at the same positions using the tree code FALCON with softening kernel P_2 and fixed softening length $\epsilon = 10^{-2}$. The RMS fractional error in the resulting accelerations for radii $2^{-5} < r < 1$ is 0.011, over four times larger than GROMMET's, while for $r < 2^{-5}$, the calculated accelerations become systematically too low. FALCON takes about 2.5 times longer than GROMMET to produce these results and needs more than three times the memory.

Perhaps the most worrying feature of the nested box scheme of section 2 is that the accelerations (3) are discontinuous at box boundaries. One can see some hints of this discontinuity in figure 3 at $\log_2 r = -1, -2, -3$, but it is even clearer in figure 4 which plots the fractional errors in a 10^8 -particle realization. Even if one were to run a simulation with such large N , the discontinuity itself is unlikely to be important because the integration scheme in section 3 does not depend explicitly on the derivatives of the accelerations (but the discontinuity does mean that the integrator is not symplectic, as noted earlier). More important is the fact that if the discontinuity is noticeable it means that the bias in the estimates of the accelerations has become significant. The natural solution is then to move to a finer mesh (e.g., 124^3 cells instead of 60^3 , figure 4).

4.2 Dynamical tests

For the dynamical tests I use a spherical isotropic Hernquist (1990) model with density profile

$$\rho(r) = \frac{Ma}{2\pi r(a+r)^3}. \quad (12)$$

This idealized model is in equilibrium. Then by Jeans' theorem (Binney & Tremaine 1987) its DF $f_0(\mathbf{x}, \mathbf{v})$ can depend on (\mathbf{x}, \mathbf{v}) only through the integrals of motion, which are the energy \mathcal{E} and angular momentum \mathbf{J} per unit mass. Since the model is isotropic the DF cannot depend on the latter and so $f = f_0(\mathcal{E})$.

A straightforward procedure for generating initial conditions (hereafter ICs) corresponding to this model would be to draw N particles directly from $f_0(\mathcal{E})$, assigning each a mass M/N . Integrating (12), the fraction of particles inside radius r would then be $r^2/(a+r)^2$, showing that there would be relatively few particles with radii $r \ll a$, deep inside the interesting r^{-1} central density cusp. To improve resolution near the centre, I instead generate initial conditions using a multi-mass scheme, drawing particles from an anisotropic sampling DF (Leeuwin, Combes & Binney 1993) with *number* density

$$f_s(\mathcal{E}, J^2) = h(\mathcal{E}, J^2)f_0(\mathcal{E}), \quad (13)$$

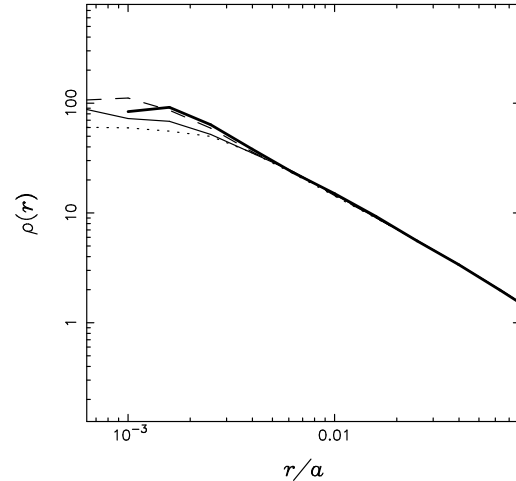


Figure 5. Inner density profile of the same realization of a Hernquist model after it has been evolved for 10 time units using a simple leapfrog integrator with accelerations obtained using different potential solvers: GROMMET (light solid curve), FALCON (dotted curve) and the SCF method (dashed). The heavy solid curve plots the density profile of the the initial conditions.

where (Sigurdsson, Hernquist & Quinlan 1995)

$$h(\mathcal{E}, J^2) \equiv A \times \begin{cases} \left(\frac{r_{\text{peri}}}{a}\right)^{-\lambda} & \text{if } r_{\text{peri}} < a, \\ 1 & \text{otherwise,} \end{cases} \quad (14)$$

$r_{\text{peri}}(\mathcal{E}, J^2)$ is the particle's pericentre radius and the constant A is chosen to normalize f_s . When the parameter $\lambda = 0$, the sampling DF f_s is identical to $f_0(\mathcal{E})$. Increasing λ improves the sampling of the cusp by increasing the number density of particles having pericentres $r_{\text{peri}} < a$. To balance this increase in number density each particle is assigned a mass $M f_0/N f_s = M/N h(\mathcal{E}, J^2)$ so that the phase-space mass density is still given by the desired $f_0(\mathcal{E})$.

For the tests below I adopt units $G = M = a = 1$ and draw 2×10^6 particles with radii in the range $10^{-3} < r < 10^2$ from the sampling DF (13) with $\lambda = 1$. Poisson noise in the resulting distribution of particles makes it slightly asymmetric, which has two unwanted consequences (see also McMillan & Dehnen 2005). First, the centre of mass of the system moves with a constant velocity of order $\sim 10^{-3}(GM/a)^{1/2}$ because the total linear momentum of the particles is small, but non-zero. Second, the asymmetry quickly destroys the inner part of the r^{-1} density cusp, even when viewed a frame co-moving with the centre of mass. To remove both of these effects, I extend my ICs to include the mirror distribution obtained by reflecting each of the 2×10^6 particles with $(\mathbf{x}, \mathbf{v}) \rightarrow (-\mathbf{x}, -\mathbf{v})$. The full ICs then have $N = 4 \times 10^6$ particles.

4.2.1 Evolution of an (almost) equilibrium model

Of course, one does not expect an N -body model evolved from these ICs to be in perfect equilibrium; the ICs omit particles outside the range $10^{-3} < r < 10^2$ and are constructed assuming the exact potential corresponding to the density distribution (12) instead of the softened potential used in the N -body code. Nevertheless, it is interesting to

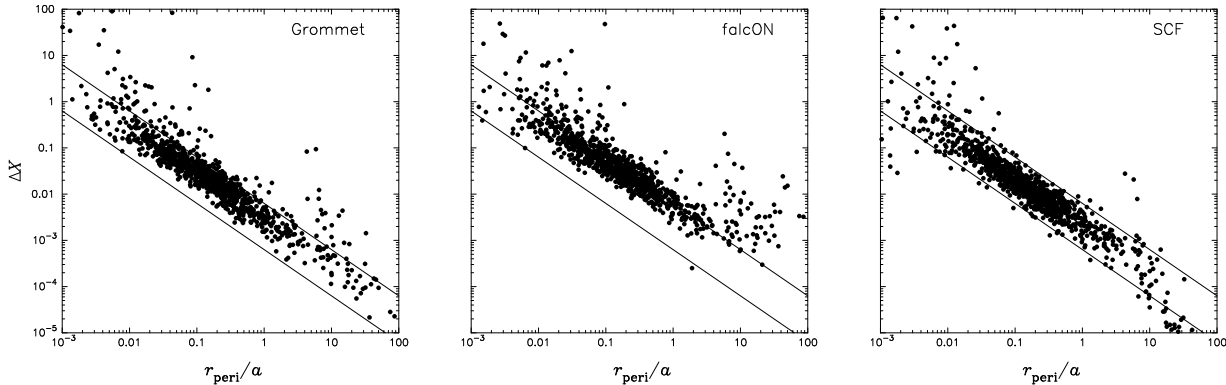


Figure 6. RMS fractional change in the angular momenta of particles in the models of figure 5, measured from $t = 0$ to $t = 10$ and plotted as a function of the particles’ pericentre radii. The same random selection of particles is used to generate each panel.

compare the evolution of the N -body model obtained from GROMMET with those obtained from the other two codes.

Figure 5 shows the density profile of the models after 10 time units (or ~ 66 circular orbit periods at $r = 0.01$). All three models use the same simple leapfrog integrator with timestep 2×10^{-3} ; only the source of the accelerations is different. For GROMMET I use boxes with boundaries at $|\mathbf{x}| = 100 \times 2^{-i}$ for $i = 0, \dots, 12$. Each box has 60^3 assignable cells, the cell length varying from 3.33 in the toplevel box down to 0.8×10^{-3} in the innermost box. FALCON’s results are obtained using kernel P_2 with softening length $\epsilon = 10^{-3}$, while the SCF expansion uses the Hernquist & Ostriker (1992) basis function expansion truncated at $n_{\max} = 6$ radial and $l_{\max} = 4$ angular terms.

The results in figure 5 are unsurprising. The density at the very centre of the GROMMET and FALCON models falls slowly because the ICs omit particles with radii $r < 10^{-3}$ and do not take into account the softening in these codes. In contrast, the density profile of the SCF model does not change significantly because its basis function expansion is incapable of producing anything that deviates strongly from a Hernquist model on small spatial scales.

Much more is happening at the level of individual orbits, however. All of these models begin with spherical symmetry and remain spherical, apart from the effects of Poisson noise. Therefore the amount of diffusion in the angular momentum J of their particles’ orbits serves as a convenient measure of how far each code is from being perfectly collisionless. Figure 6 shows that the particles in all three models suffer from significant amounts of diffusion. The SCF model shows the least diffusion, but it is only marginally better than GROMMET; although the SCF potential remains close to the exact Hernquist potential, the flickering of the expansion coefficients with time makes the orbits diffuse just like in any other code. The diffusion is worst in the FALCON model, particularly for orbits having pericentres much larger than its fixed softening length $\epsilon = 10^{-3}$. All of these results are based on the variation in orbits’ angular momentum in models integrated from $t = 0$ to $t = 10$, but I find similar results for models integrated from, say, $t = 10$ to $t = 50$ when scaled to account for the longer timescale over which the diffusion occurs.

The results presented so far have been obtained using an integrator with a single small timestep, but the dynamical

Code	Time	Comment
FALCON	2.1	single timestep
SCF	1.3	single timestep, $(n_{\max}, l_{\max}) = (6, 4)$
GROMMET	1.0	single timestep
GROMMET	0.3	four levels of timestep refinement
GROMMET	0.16	seven levels of timestep refinement

Table 1. Comparison of time required for different codes to integrate the multi-mass Hernquist model of section 4.2, relative to the single-timestep implementation of GROMMET. Neither the GROMMET nor the SCF models take advantage of the reflection symmetry of this simple problem.

time inside the cusp of a Hernquist model varies with radius r approximately as $r^{1/2}$. As, e.g., Zemp et al. (2007) have argued, it is natural to advance particles using a timestep proportional to the local dynamical time. We can come close to the optimal $\tau \propto r^{1/2}$ scaling by using the block-timestep integrator of section 3.2 above and halving the timestep on every second subbox. To test the practicality of this scheme, I have run a model with timesteps $\tau = 32 \times 10^{-3}$ for particles with $|\mathbf{x}| > 100 \times 2^{-6} \simeq 1.5$, shrinking by a factor of two at the boundaries $|\mathbf{x}| = 100 \times 2^{-i}$ of boxes $i = 6, 8, 10$ and 12 . In the innermost ($i = 12$) box the timestep is 2×10^{-3} , the same used for the single-timestep run above. This multiple-timestep model yields results almost indistinguishable from the single-timestep GROMMET model plotted in figures 5 and 6, but is three times faster (see table 1). If it were appropriate to halve the timestep at *all* box boundaries $i = 6, \dots, 12$ (see below for an example) then the block-timestep scheme would yield a sixfold increase in speed over the single-timestep integrator.

4.2.2 Response to an adiabatically grown blob

For a slightly more interesting test, I model the growth of a black hole at the centre of a galaxy by slowly adding a Plummer sphere potential

$$\Phi_b(\mathbf{x}; t) = -\frac{GM_b(t)}{\sqrt{r^2 + b^2}} \quad (15)$$

to a multi-mass Hernquist model. The scale radius of the Plummer sphere $b = 2 \times 10^{-3}$ and its mass grows with time

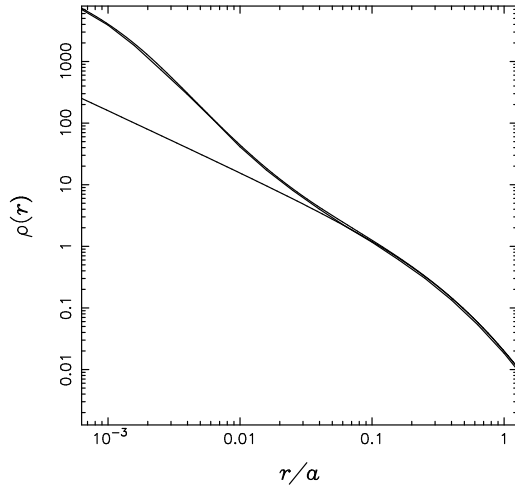


Figure 7. The results of adiabatically adding a Plummer sphere potential to an initially isotropic Hernquist model. The Plummer sphere has radius $2 \times 10^{-3}a$ and a final mass $2 \times 10^{-3} M_{\text{gal}}$. The results obtained using GROMMET's multiple-timestep scheme are almost identical to those calculated from Young's (1980) method.

as (Sigurdsson, Hernquist & Quinlan 1995)

$$M_b(t) = M_f \times \begin{cases} \left[3 \left(\frac{t}{t_g} \right)^2 - 2 \left(\frac{t}{t_g} \right)^3 \right] & \text{if } t < t_g \\ 1 & \text{otherwise,} \end{cases} \quad (16)$$

its final mass $M_f = 2 \times 10^{-3}$ being reached in a time $t_g = 5$.

A safe, formal way of including the effects of this external potential in GROMMET is to add an extra term

$$\sum_{k=-\infty}^{\infty} \delta_{\epsilon} \left(k - \frac{t}{2^{-l_{\max}} \tau_0} \right) \sum_{i=1}^N m_i \Phi_b(\mathbf{x}_i; t) \quad (17)$$

to the Hamiltonian (10). Integrating the resulting equations of motion then leads to the modifications needed in the block-timestep algorithm (section 3.2). In this case the necessary modifications are obvious, but for more realistic situations (e.g., if the mass of the external source did not change in time and if the location of its centre were not pinned to $\mathbf{x} = 0$) then it is helpful to start from (10) to ensure that the perturbation is turned on at the appropriate times and momentum conserved.

As above, I use a nested series of boxes with boundaries at $|\mathbf{x}| = 100 \times 2^{-i}$ with $i = 0, \dots, 12$, each box covered by a 60^3 mesh. Boxes 0 to 5 share a common timestep $\tau_0 = 5 \times 10^{-3}$. This is refined in every subsequent box, so that the timestep associated with box $i \geq 6$ is $2^{5-i} \tau_0$ and the innermost box ($|\mathbf{x}| < 0.024$) has timestep $\sim 4 \times 10^{-5}$.

My initial conditions consist of 10^6 particles drawn from the sampling DF (13) above. The artificially imposed potential at $\mathbf{x} = 0$ means that this simulation only makes sense if the particles' centre of mass is also at $\mathbf{x} = 0$. As an alternative to symmetrizing the ICs as before, I instead modify step (i) of the PM method (section 2) to reflect the particle distribution through each of the planes $\mathbf{x} = 0$, $\mathbf{y} = 0$, $\mathbf{z} = 0$ when assigning mass to meshes. This increases the effective N used for the potential by a factor of 8 at little cost. The density profile of the final model is plotted in figure 7.

It agrees well with the predictions obtained using Young's (1980) method.

5 SUMMARY

I have described GROMMET, a fast, economical particle-multiple-mesh N -body code designed specifically for modelling the dynamical evolution of individual galaxies. In other words, it is designed to tackle almost exactly the same type of problem to which the SCF method (Hernquist & Ostriker 1992) is applied. Indeed, GROMMET can – loosely – be thought of as a variant of the SCF method using a Cartesian basis function expansion with millions of expansion coefficients (the density at each mesh vertex in each of the nested boxes). Any application of the SCF method requires that one make a careful choice of the basis functions used to represent the density and potential. Similarly, in GROMMET one has to choose, by hand, the set of nested boxes to use.

For a realistic model galaxy with $N \gtrsim 10^6$, the single-timestep incarnation of GROMMET is comparable in speed to an SCF code using a low-order basis expansion and shows comparable amounts of relaxation. For most applications, however, GROMMET will be much faster: its nested-box potential solver admits an efficient natural block-timestep integrator (section 3.2), leading to an approximate three- to six-fold increase in speed for realistic galaxy models; the SCF method typically requires a fairly high-order expansion to produce (reasonably) unbiased results (e.g., Holley-Bockelmann, Weinberg & Katz 2005), which makes it much slower in practice. But perhaps the main advantage of GROMMET over SCF methods based on spherical harmonic expansions is that it respects Newton's third law and is therefore suitable for use in studying $l = 1$ perturbations without fear of artefacts due to centring.

To my knowledge, the tree code FALCON (Dehnen 2002) is the only other code that can model realistically inhomogeneous galaxies without breaking the third law. For $N \gtrsim 10^6$ GROMMET's potential solver is more than twice as fast as FALCON's and much less memory hungry. This efficiency comes at a cost though, since GROMMET's nested-box scheme is optimized for modelling perturbations of single galaxies. It would be interesting to see whether the potential-splitting scheme used here (section 3.2; Duncan, Levison & Lee (1998)) works as well for FALCON, or indeed any other code that respects the third law, as it does for GROMMET.

ACKNOWLEDGMENTS

I thank James Binney, Walter Dehnen and Ben Moore for helpful discussions, and the Royal Society for financial support.

REFERENCES

- Anninos P., Norman M. L., Clarke D. A., 1994, *ApJ*, 436, 11
- Binney J., Tremaine S., 1987, *Galactic Dynamics*, Princeton Univ. Press, Princeton, NJ
- Dehnen W., 2002, *J. Comput. Phys.*, 179, 27

- Duncan M. J., Levison H. F., Lee M. H., 1998, *AJ*, 116, 2067
- Gelato S., Chernoff D. F., Wasserman I., 1997, *ApJ*, 480, 115
- Hernquist L., 1990, *ApJ*, 356, 359
- Hernquist L., Ostriker J. P., 1992, *ApJ*, 386, 375
- Hernquist L., Weinberg M. D., 1989, *MNRAS*, 238, 407
- Hockney R. W., Eastwood J. W., *Computer simulation using particles*, 1988, IoP
- Holley-Bockelmann K., Weinberg M., Katz N., 2005, *MNRAS*, 363, 991
- James R. A., 1977, *J. Comp. Phys.*, 25, 71
- Jessop C., Duncan M., Chau, W. Y., 1994, *J. Comput. Phys.*, 115, 339
- Knebe A., Green A., Binney J., 2001, *MNRAS*, 325, 845
- Kravtsov A. V., Klypin A. A., Khokhlov A. M., 1997, *ApJS*, 111, 73
- Lauer T. R., et al., 1995, *AJ*, 110, 2622
- Leeuw F., Combes F., Binney J., 1993, *MNRAS*, 262, 1013
- McMillan P. J., Dehnen W., 2005, *MNRAS*, 363, 1205
- Saha P., Tremaine S., 1992, *AJ*, 104, 1633
- Sigurdsson S., Hernquist L., Quinlan G. D., 1995, *ApJ*, 446, 75
- Velazquez H., White S. D. M., 1999, *MNRAS*, 304, 254
- Weinberg M. D., 1989, *MNRAS*, 239, 549
- Wisdom J., Holman M., 1991, *AJ*, 102, 1528
- Young P., 1980, *ApJ*, 242, 1232
- Zemp M., Stadel J., Moore B., Carollo C. M., 2007, *MNRAS*, 376, 273

APPENDIX A: JAMES' METHOD

James (1977) describes an economical method for calculating the solution to Poisson's equation,

$$\nabla^2 \Phi = -q, \quad (\text{A1})$$

discretized on a regular mesh and with a spatially bounded source distribution $q(\mathbf{x})$, so that $\partial\Phi/\partial r \rightarrow 0$ as $r \rightarrow \infty$. It is easiest to explain his method for the electrostatic case in which q is electric charge density and Φ is electrostatic potential. The method then consists of the following steps:

- (i) enclose the charge distribution q inside an earthed metal box and calculate the potential $\phi(\mathbf{x})$ inside the box subject to the boundary condition $\phi = 0$ on the box surface;
- (ii) use Gauss' law to find the charge distribution Q induced on the surface of the box;
- (iii) calculate the potential $\psi(\mathbf{x})$ due to this surface charge distribution Q .

The solution to (A1) for the isolated charge distribution q is given by $\Phi = \phi - \psi$. Since this procedure is at the heart of GROMMET's potential solver, I explain it in some detail below.

A1 Preliminaries

Throughout the following, I assume that the distribution $q(\mathbf{x})$ has been discretized onto a cubical mesh with vertices

at positions $\mathbf{x}_{ijk} = (i, j, k)$, $0 \leq i, j, k \leq n$, spaced unit distance apart. Our goal is to calculate the discretized potential Φ_{ijk} corresponding to this q_{ijk} .

A straightforward way of doing this is to use the Fourier convolution theorem. Consider first the situation in which the charge distribution q_j is one-dimensional with $0 \leq j < 2n$; the reason for extending the mesh from $n+1$ to $2n$ vertices will become apparent shortly. The discretized potential is given by the convolution

$$\Phi_j = \sum_{k=0}^{2n-1} G_k q_{k-j}, \quad (\text{A2})$$

where G_k is the contribution to Φ_k made by a unit-charge particle located at x_0 , and we take $q_k = 0$ for $k < 0$ or $k \geq 2n$ since we have an isolated charge distribution.

This last condition on q is awkward. Suppose instead that both that G_k and q_k were $2n$ -periodic, with $q_{-k} = q_{2n-k}$, and let us impose the sensible condition that G_k is even with $G_k = G_{2n-k}$ and that $G_0 = 0$. Then Φ_j could be obtained economically using Fourier methods. The Fourier transform of q_i is given by

$$q^\alpha \equiv \sum_{j=0}^{2n-1} q_j \exp \left[\frac{i\pi j\alpha}{n} \right], \quad (\text{A3})$$

where $i \equiv \sqrt{-1}$, and similarly for G^α . Using the discrete convolution theorem, equation (A2) becomes simply

$$\Phi^\alpha = G^\alpha q^\alpha. \quad (\text{A4})$$

Applying the inverse transform, the potential is given by

$$\Phi_j = \frac{1}{2n} \sum_{\alpha=0}^{2n-1} \Phi^\alpha \exp \left[-\frac{i\pi j\alpha}{n} \right]. \quad (\text{A5})$$

The periodicity needed for application of the discrete convolution theorem is a nuisance, but if we allow q_i to be non-zero only for $0 \leq i \leq n$, then the $\Phi_0 \dots \Phi_n$ obtained from equ. (A2) are unaffected by it. Therefore, we can use this Fourier method to obtain the potential Φ_i corresponding to an isolated source distribution q_i ($0 \leq i \leq n$) provided we extend the mesh by a further $n-1$ points with $q_{n+1} = \dots = q_{2n-1} = 0$. Thanks to the existence of fast methods for evaluating the transforms (A3) and (A5), the Fourier method requires only $\mathcal{O}(n \log n)$ operations to calculate the full set of Φ_i , instead of the $\mathcal{O}(n^2)$ involved in a direct evaluation of equ. (A2). The savings are much more dramatic for the three-dimensional case, for which the direct sum takes $\mathcal{O}(n^6)$ operations, compared to only $\mathcal{O}((n \log n)^3)$ for the Fourier method.

James' method makes use of an alternative view of this "doubling up" procedure. The Fourier transform (A3) can be written as

$$q^\alpha = 2[q^\alpha(C) + iq^\alpha(S)], \quad (\text{A6})$$

where the cosine and sine transforms

$$q^\alpha(C) \equiv \sum_{j=0}^n c_j q_j \cos \frac{\pi j\alpha}{n}, \quad (\text{A7})$$

$$q^\alpha(S) \equiv \sum_{j=1}^{n-1} q_j \sin \frac{\pi j\alpha}{n}, \quad (\text{A8})$$

come from the even and odd parts of q_j ,

$$q_j^\pm \equiv \frac{1}{2} (q_j \pm q_{2n-j}), \quad (\text{A9})$$

respectively. The coefficients $c_1 = \dots = c_{n-1} = 1$, but $c_0 = c_n = \frac{1}{2}$ to account for the fact that q_0 and q_n are counted only half as often as the other q_i . Conversely, having both $q^\alpha(C)$ and $q^\alpha(S)$ we can reconstruct the original q_j by substituting (A6) into the expression for the inverse transform (A5) to obtain

$$q_j = q_j(C) + q_j(S), \quad (\text{A10})$$

where

$$q_j(C) \equiv \frac{2}{n} \sum_{\alpha=0}^n c_\alpha q^\alpha(C) \cos \frac{\pi j \alpha}{n}, \quad (\text{A11})$$

$$q_j(S) \equiv \frac{2}{n} \sum_{\alpha=1}^{n-1} q^\alpha(S) \sin \frac{\pi j \alpha}{n} \quad (\text{A12})$$

are the inverse cosine and sine transforms of $q^\alpha(C)$ and $q^\alpha(S)$ respectively. Thus, apart from a factor of $(2/n)$, the cosine and sine transforms are their own inverses.

Now suppose that only $q_0 \dots q_n$ are allowed to be non-zero. Then $q_i^+ = q_i^- = q_i$, except for the unused $q_0^- = q_n^- = 0$. Replacing q by Φ in eqs. (A10-A12) and taking Φ^α from (A4), the potential can be written as

$$\Phi_j = \Phi_j(C) + \Phi_j(S), \quad (\text{A13})$$

where

$$\Phi_j(C) \equiv \frac{2}{n} \sum_{\alpha=0}^n c_\alpha G^\alpha q^\alpha(C) \cos \frac{\pi j \alpha}{n}, \quad (\text{A14})$$

$$\Phi_j(S) \equiv \frac{2}{n} \sum_{\alpha=1}^{n-1} G^\alpha q^\alpha(S) \sin \frac{\pi j \alpha}{n}, \quad (\text{A15})$$

and $G^\alpha = 2G^\alpha(C)$ with no contribution from the sine transform of the even function G_i .

The generalization to three dimensions is straightforward. The Fourier transform in each direction splits into a sum of cosine and sine terms, yielding a total of eight terms:

$$\begin{aligned} \Phi_{ijk} = & \Phi_{ijk}(CCC) + \Phi_{ijk}(CCS) + \Phi_{ijk}(CSC) \\ & + \Phi_{ijk}(CSS) + \Phi_{ijk}(SCC) + \Phi_{ijk}(SCS) \\ & + \Phi_{ijk}(SSC) + \Phi_{ijk}(SSS), \end{aligned} \quad (\text{A16})$$

where, for example,

$$\begin{aligned} \Phi_{ijk}(CSS) \equiv & \frac{8}{n^3} \sum_{i=0}^n \sum_{j=1}^{n-1} \sum_{k=1}^{n-1} c_i \Phi^{\alpha\beta\gamma}(CSS) \times \\ & \cos \frac{\pi i \alpha}{n} \sin \frac{\pi j \beta}{n} \sin \frac{\pi k \gamma}{n}, \end{aligned} \quad (\text{A17})$$

with $\Phi^{\alpha\beta\gamma}(CSS) = G^{\alpha\beta\gamma} q^{\alpha\beta\gamma}(CSS)$ and

$$q^{\alpha\beta\gamma}(CSS) \equiv \sum_{i=0}^n \sum_{j=1}^{n-1} \sum_{k=1}^{n-1} c_i q_{ijk} \cos \frac{\pi i \alpha}{n} \sin \frac{\pi j \beta}{n} \sin \frac{\pi k \gamma}{n}. \quad (\text{A18})$$

Notice that this decomposition into sine and cosine transforms results in two transforms for each of eight n^3 meshes. It requires less memory than the equivalent single $(2n)^3$ zero-padded mesh used in the “doubling-up” procedure, but for

general q_{ijk} and G_{ijk} it offers no improvement in speed. It simplifies enormously, however, for the special case in which G_{ijk} is the Green’s function of the discretized Laplacian appearing in equ. (A1). James’ method exploits these simplifications, particularly in dealing with the hollow induced surface charge distribution Q (see section A4 below).

A2 The potential of a charge distribution inside an earthed box

With this background in hand, let us turn to the details of James’ method. Poisson’s equation (A1) can be written

$$(\Delta\Phi)_{ijk} = -q_{ijk} \quad (\text{A19})$$

where the first-order approximation to the Laplacian operator

$$\begin{aligned} (\Delta\Phi)_{ijk} \equiv & \Phi_{i+1,j,k} + \Phi_{i-1,j,k} + \Phi_{i,j+1,k} + \Phi_{i,j-1,k} + \\ & + \Phi_{i,j,k+1} + \Phi_{i,j,k-1} - 6\Phi_{ijk}. \end{aligned} \quad (\text{A20})$$

The potential ϕ_{ijk} of the earthed box is given by the solution of this equation subject to the boundary condition $\phi_{0jk} = \phi_{njk} = \phi_{i0k} = \phi_{ink} = \phi_{ij0} = \phi_{ijn} = 0$. Applying the triple sine transform, we have that

$$\phi^{\alpha\beta\gamma}(SSS) = q^{\alpha\beta\gamma}(SSS)/C^{\alpha\beta\gamma} \quad (\text{A21})$$

where

$$C^{\alpha\beta\gamma} = 2 \left(1 - \cos \frac{\pi \alpha}{n} \right) + 2 \left(1 - \cos \frac{\pi \beta}{n} \right) + 2 \left(1 - \cos \frac{\pi \gamma}{n} \right). \quad (\text{A22})$$

Although we could immediately apply the inverse transform (A16) to obtain ϕ_{ijk} explicitly, it turns out that this is unnecessary and it is more efficient to use the method of equivalent charges (see below) to modify $\phi^{\alpha\beta\gamma}(SSS)$ to include the effects of the potential ψ corresponding to the induced surface charge distribution Q , saving everything for a single inverse transform at the very end of the calculation.

A3 The charge distribution induced on the faces of the box

The charge distribution induced on the $i = 0$ face of the box is given by

$$Q_{0jk} = -(\Delta\phi)_{0jk} = -\phi_{1jk}, \quad (\text{A23})$$

the last equality following from the fact that ϕ is zero both on the box surface ($i = 0$) and outside the box ($i = -1$). Similarly, the charge distribution induced on the opposite $i = n$ face is $Q_{njk} = \phi_{n-1,jk}$. Notice that Q vanishes along the edges of the box, and so is completely specified by its double sine transform on each of the six faces. In terms of $\phi^{\alpha\beta\gamma}(SSS)$ these can be written

$$Q_0^{\beta\gamma}(SS) = \frac{2}{n} \sum_{\alpha=1}^{n-1} \phi^{\alpha\beta\gamma}(SSS) \sin \frac{\pi \alpha}{n}, \quad (\text{A24})$$

$$Q_n^{\beta\gamma}(SS) = \frac{2}{n} \sum_{\alpha=1}^{n-1} (-1)^\alpha \phi^{\alpha\beta\gamma}(SSS) \sin \frac{\pi \alpha}{n}, \quad (\text{A25})$$

and similarly for the other four faces. We can invert each of these to obtain Q_{0jk} etc and, from these, any of the other three transforms $Q_0^{\beta\gamma}(SC)$, $Q_0^{\beta\gamma}(CC)$, $Q_0^{\beta\gamma}(CS)$.

A4 The potential of the induced charge distribution

Equation (A16) provides a way of obtaining the potential ψ_{ijk} corresponding to this induced charge distribution Q . The result is a sum of eight terms, all of which can be treated in the same way. For example, consider the term $\psi_{ijk}(CSS)$. Its Fourier transform $\psi^{\alpha\beta\gamma}(CSS) = G^{\alpha\beta\gamma}Q^{\alpha\beta\gamma}(CSS)$, where, using (A18) and the hollowness of Q ,

$$Q^{\alpha\beta\gamma}(CSS) = Q_0^{\beta\gamma}(SS) + (-1)^\alpha Q_n^{\beta\gamma}(SS). \quad (\text{A26})$$

The other terms can be written in a similar way, although the SSS term vanishes. The $G^{\alpha\beta\gamma}$ used here should be the triple cosine transform of the Green's function for the first-order Laplacian (A20). This need be calculated just once (e.g., using the doubling-up procedure), the necessary elements being stored for subsequent use.

It would be possible to use eq. (A16) to obtain ψ_{ijk} directly, but it turns out (see below) that this labour is unnecessary and that it suffices to use (A16) to obtain only the face potentials ψ_{0jk} , ψ_{njk} etc. Nevertheless, adding up all the contributions to each of these turns out to be the main computational burden of James' method.

A5 The method of equivalent charges

Instead of synthesizing ψ_{ijk} explicitly, let us introduce another potential $\psi_{ijk}^{(E)}$ which is zero on the box faces but everywhere else is equal to ψ_{ijk} . Because it vanishes at the box boundaries, this new potential is completely specified by its triple sine transform. The "equivalent charge" distribution E_{ijk} that generates it can be found using Poisson's equation

$$\nabla^2 [\psi - \psi^{(E)}] = -[Q - E], \quad (\text{A27})$$

where Q is non-zero only on the faces of the box. For the first-order discretized Laplacian (equ. A20) E is confined to the planes $i = 1, j = 1, k = 1, i = n - 1, j = n - 1$ and $k = n - 1$, with, for example, $E_1^{\beta\gamma}(SS) = \psi_0^{\beta\gamma}(SS)$.

The triple sine transform of the full potential is then

$$\Phi^{\alpha\beta\gamma}(SSS) = \phi^{\alpha\beta\gamma}(SSS) - E^{\alpha\beta\gamma}(SSS)/C^{\alpha\beta\gamma} \quad (\text{A28})$$

the second term giving the contribution of $\psi^{(E)}$. Applying the inverse triple-sine transform to (A28) gives Φ_{ijk} for $1 \leq i, j, k < n$. Finally, the missing face potentials can be inserted using the results obtained in section A4.

A6 Performance

My implementation of this procedure uses the fast sine and cosine transforms written by Takuya Ooura.² The triple-sine transforms involved in going from q_{ijk} to $\phi^{\alpha\beta\gamma}(SSS)$ (eq. A21) and from $\Phi^{\alpha\beta\gamma}(SSS)$ to Φ_{ijk} (eq. A28) then take only $\sim 30\%$ of the total time needed to go from q_{ijk} to Φ_{ijk} , with the evaluation of the various transforms of the face charge distributions (Sec. A3) accounting for a further 10%. The remaining 60% of the time is spent simply accumulating the various contributions to the face potentials (sec. A4). Nevertheless, for typical 65^3 or 129^3 meshes I find that my

implementation of James' method is about 60 to 70% faster than the usual doubling-up procedure.

I have focused here on describing James' method using the first-order approximation of the Laplacian (A20). James (1977) shows how it is possible to apply the same ideas to higher-order approximations, albeit at the expense of much more involved book-keeping. I find that the resulting minor changes in the Green's function G_{ijk} have no detectable effect for the realistic large- N situations described in section 4.

² <http://kurims.kyoto-u.ac.jp/~ooura/fft.html>